

NASA Technical Memorandum

NASA TM - 100373

STATIC AND DYNAMIC DEFLECTION STUDIES OF THE SRM AFT CASE/NOZZLE JOINT

By David C. Christian, Lawrence D. Kos, and Isaias Torres

Structures and Dynamics Laboratory
Science and Engineering Directorate

August 1989

(NASA-TM-100373) STATIC AND DYNAMIC
DEFLECTION STUDIES OF THE SRM AFT
CASE-NOZZLE JOINT (NASA. Marshall Space
Flight Center) 37 p
CSCL 21H

N89-28568

Unclas
63/20 0231752



National Aeronautics and
Space Administration

George C. Marshall Space Flight Center

1. REPORT NO. NASA TM-100373	2. GOVERNMENT ACCESSION NO.		3. RECIPIENT'S CATALOG NO.	
4. TITLE AND SUBTITLE Static and Dynamic Deflection Studies of the SRM Aft Case/Nozzle Joint			5. REPORT DATE August 1989	
7. AUTHOR(S) David C. Christian, Lawrence D. Kos, and Isaias Torres			6. PERFORMING ORGANIZATION CODE	
9. PERFORMING ORGANIZATION NAME AND ADDRESS George C. Marshall Space Flight Center Marshall Space Flight Center, Alabama 35812			8. PERFORMING ORGANIZATION REPORT #	
12. SPONSORING AGENCY NAME AND ADDRESS National Aeronautics and Space Administration Washington, D.C. 20546			10. WORK UNIT NO.	
15. SUPPLEMENTARY NOTES Prepared by Component Assessment Branch, Structural Analysis Division, Structures and Dynamics Laboratory, Science and Engineering Directorate.			11. CONTRACT OR GRANT NO.	
16. ABSTRACT			13. TYPE OF REPORT & PERIOD COVERED Technical Memorandum	
17. KEY WORDS Modal analysis Statics Dynamics NASTRAN Base driving response Transient response			14. SPONSORING AGENCY CODE	
18. DISTRIBUTION STATEMENT Unclassified - Unlimited			19. SECURITY CLASSIF. (of this report) Unclassified	
20. SECURITY CLASSIF. (of this page) Unclassified			21. NO. OF PAGES 38	22. PRICE NTIS

TABLE OF CONTENTS

	Page
I. INTRODUCTION	1
A. Background	1
B. Purpose	2
II. MODEL DEVELOPMENT	3
III. THEORETICAL TREATMENT: ASSUMPTIONS AND EQUATIONS	5
A. Direct Transient Response Analysis	8
B. Static Analysis	8
C. Base Driving Response Analysis	9
IV. TYPES OF ANALYSES	10
A. Modal Analysis	10
B. Static Analysis	16
C. Transient Response Analysis	16
D. Base Driving Response Analysis	18
V. RESULTS	18
A. Model Verification with TPTA Test Results	18
B. Analysis Results	20
VI. CONCLUSIONS AND RECOMMENDATIONS	25
APPENDIX	27
REFERENCES	33

LIST OF ILLUSTRATIONS

Figure	Title	Page
1.	SRB aft dome/nozzle joint	2
2.	Current joint design	3
3.	SRB aft dome/nozzle joint dynamic model	4
4.	X-location of gridpoints in gap	5
5.	Base driving analysis flow chart.....	11
6.	Modal deformation: Mode 1, frequency 2.22 Hz.....	12
7.	Modal deformation: Mode 2, frequency 14.73 Hz	13
8.	Modal deformation: Mode 3, frequency 15.27 Hz	13
9.	Modal deformation: Mode 4, frequency 22.28 Hz	14
10.	Modal deformation: Mode 5, frequency 22.32 Hz	14
11.	Modal deformation: Mode 6, frequency 65.47 Hz	15
12.	Modal deformation: Mode 7, frequency 185.5 Hz	15
13.	Measured pressure on aft SRM dome.....	17
14.	Base driving forcing function X-direction	19
15.	Base driving forcing function Y-direction	19
16.	Base driving forcing function Z-direction.....	19
17.	Static gap between fixed housing and aft dome – TPTA test	20
18.	Static gap between fixed housing and aft dome – flight math model	21
19.	Static deflected model compared with undeflected model	21
20.	Gap deflections with and without radial bolts	22
21.	Transient analysis gap deflections	23
22.	Relative vibration gap motion at aft dome/fixed housing (X-direction).....	24

TECHNICAL MEMORANDUM

STATIC AND DYNAMIC DEFLECTION STUDIES OF THE SRM AFT CASE/NOZZLE JOINT

I. INTRODUCTION

A. Background

Recently, there has been an increasing interest in efficiently developing large math model configurations for dynamic and static analyses. The prediction of the behavior of a structure is generally based upon the results of the analysis of a mathematical model of the structure. The accuracy of this prediction depends on how well the model approximates the structural characteristics. For this reason, it is important to know the limitations of modeling procedures, the software, and the model developed to represent the structure.

The rapid development of computers has completely transformed research and engineering practices in every technical field, particularly in the field of structural dynamic analysis. Conventional computers have rapidly branched out into supercomputers, minicomputers, and graphics computers and workstations. Personal computers today are as common as calculators were in the 1970's and slide rules in the 1960's and before. Microcomputers are being developed with unprecedented memory, speed, and graphics capabilities. Most of the math modeling experience has been accumulated in the last two decades primarily because of the development of and increase in the use of computers.

Math model characteristics should be similar to that of the physical structure. Models are used to plan, design, and study the physical structure. In most cases, modeling and analysis of the model reduces the cost, risk, and the amount of time required to accomplish these tasks. Frequently, math modeling of the structure is the only way to do this because the hardware may be unusable or unavailable for testing or for other purposes.

In order to resolve problems using math models, it is necessary to understand the system (or structure) and the problems relating to that system. Math models should be developed, from the start, with a specific problem or set of problems in mind to facilitate best use of the model. The software used to translate the model into a form usable by these newer generation computers must also be a suitable vehicle to perform this task. The results (output) should also be able to be analyzed and correctly interpreted such that engineering decisions to resolve the problem can be made. The success of a modeler depends on how well he/she can define significant elements of the problem, establish the relationship between each part, and obtain meaningful and accurate information from the model. This report presents a technical study of this type for the solid rocket motor (SRM) aft dome/nozzle for the Space Shuttle vehicle.

B. Purpose

Several types of structural dynamic and static response analyses were performed on the SRM aft case/nozzle joint, with all the results from these studies being presented in this report. The main purpose of this study was to determine gap deflections at the joint caused by the chamber pressure, nozzle blowout forces, actuator gimbal loads, and vehicle low-frequency vibration accelerations. The computed data is compared with test data to verify the model of the SRM structure.

The location and configuration of the joint can be seen on Figure 1 with the enlargement on Figure 2 showing a close-up of the joint with the new design using the radial bolts. (The old design did not include the radial bolts.) The aft dome, fixed housing, and nozzle were modeled using MacNeal Schendler NASTRAN (MSC/NASTRAN). Figure 1 shows a cross-section of these parts and their relative positions. The model was fixed in the X, Y, and Z directions at the tangent point, the tangent point being located a short distance below the aftmost factory joint on the aft segment of the SRM as shown in Figure 1.

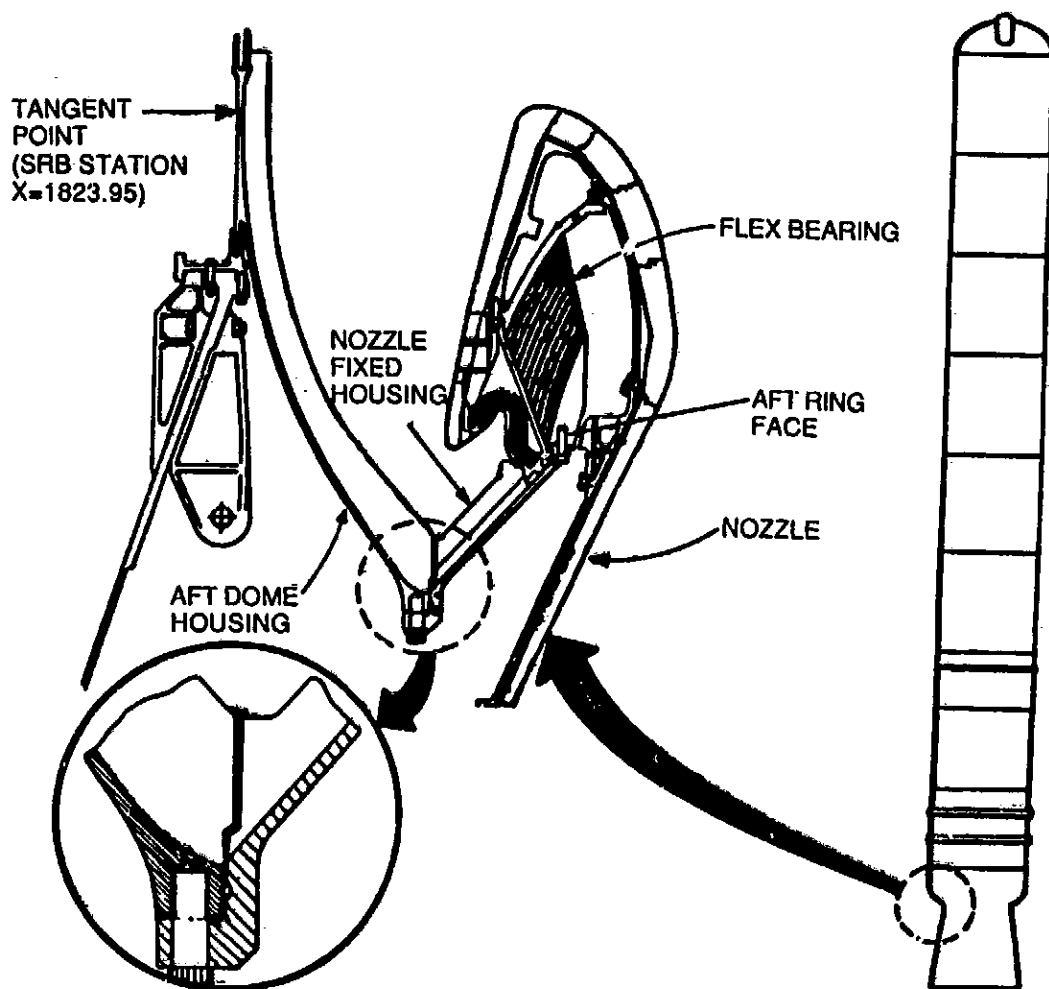
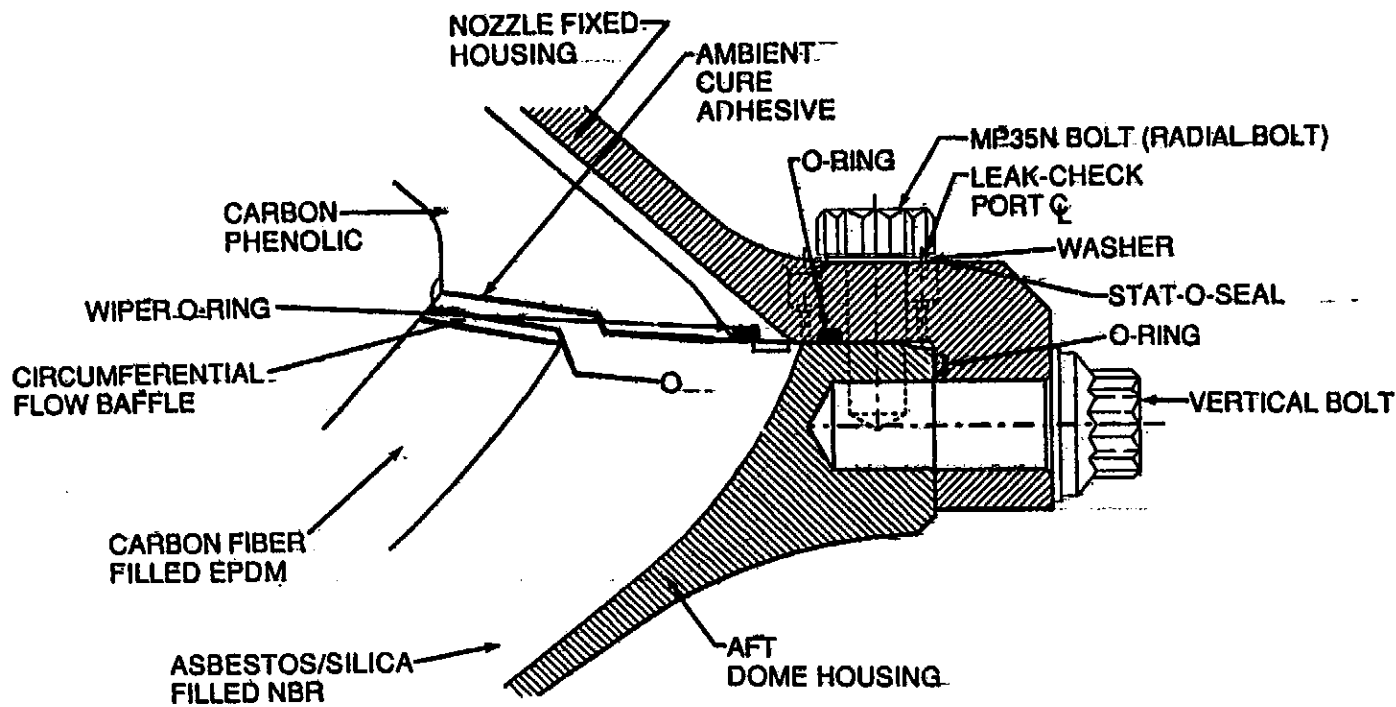


Figure 1. SRM aft dome/nozzle joint.



NOTE: RADIAL BOLT NOT USED IN ORIGINAL DESIGN.

Figure 2. Current joint design.

II. MODEL DEVELOPMENT

The analysis of the SRM aft dome/nozzle joint structure involved developing a large finite element model of the aft dome, the fixed housing, and the nozzle. The model was developed using an Intergraph Graphics Design Station (IGDS) workstation for input to MSC/NASTRAN software on the IBM/Cray computer. The structural dimensions and details were obtained from Morton Thiokol drawings noted in References 1 through 4.

An isometric view of the model is shown on Figure 3, which started with approximately 32,400 degrees-of-freedom (DOF) and then was reduced to approximately 22,050 DOF. The nozzle is modeled with beam elements and includes two rod elements for the nozzle actuators. Plate, bar, rod, and solid elements are used to model the complete joint structure. The aft skirt was not included in the math model because it is much stiffer than the aft dome, to which it is connected, so that the analysis would provide conservative results. The math model was developed in the full 360-degree configuration to allow for unsymmetrical loading and checking results in an unsymmetrical fashion to be sure the worst case was enveloped.

The model was developed with more fidelity (finer grid mesh) at the fixed housing/aft dome interface (Fig. 2) with 2,100 grids between these parts. At the SRM case tangent point, the boundary/base of the model, the model has the coarsest grid spacing with 50 stations around the circle. This spacing compares to 200 stations around the circle at the aft dome/fixed housing interface. The fixed housing and aft dome are held together with both vertical (axial) and radial

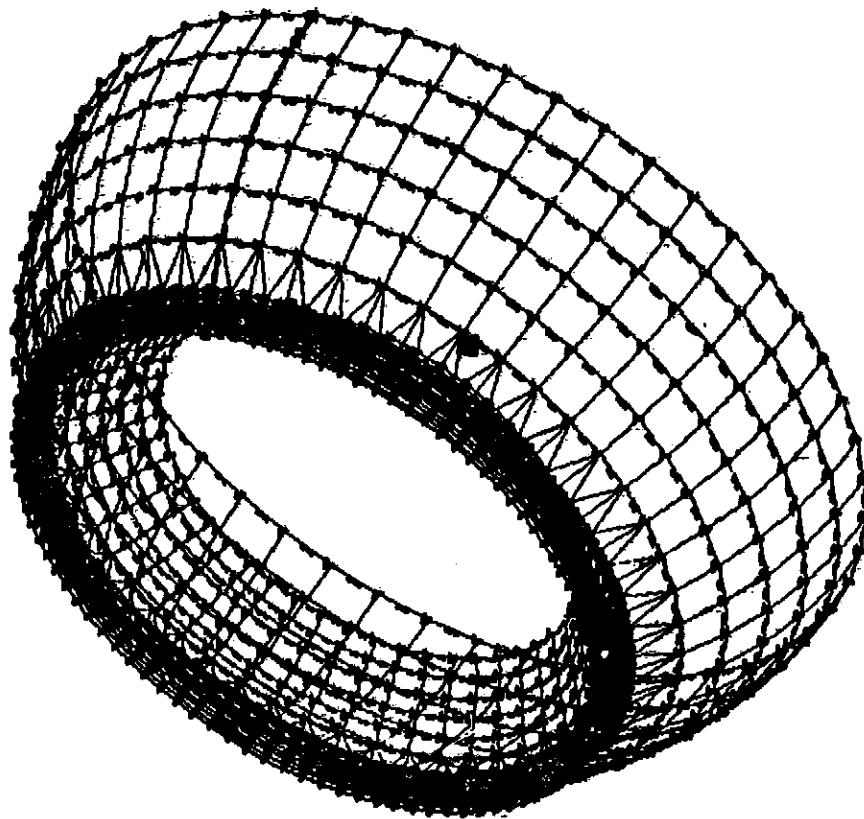


Figure 3. SRB aft dome/nozzle joint dynamic model.

bolts. These bolts are modeled with three grids and two bars, one bar which has the bolt preload applied to it. This preload helps lower the gap opening when the loads, such as the SRM internal pressure, are applied to the structure. The effects of the bolt preloads are included in the analyses results and will be evident in the data presented. The 50 boundary support points were all constrained in the three translational directions. The low frequency vibrational motion at these 50 points were available only in the three translation directions, therefore the rotational DOF's were removed from these boundary points.

The flex bearing assembly in the center area of the model and the vertical bolt area of the model (Figs. 1 and 2) were made with slightly less fidelity than the radial bolt area of the model to minimize the number of DOF and speed up the analysis time. For example, the stiffness of the flex bearing area is not directly included at the fixed housing/nozzle interface, but the nozzle part of the model was tuned to nozzle/flex bearing frequencies [5,6] to account for this flexibility in the model and match the structure's behavior. To help accomplish this step with the model, the rotational stiffnesses at the fixed housing/nozzle interface was left out to represent the flex bearing more accurately. The nozzle is represented by a cantilevered beam with dynamic characteristics similar to a larger, more detailed and complete nozzle model.

The primary purpose of the model was to provide deflections along the vertical face at the locations of the primary O-ring and the radial bolt. The modeling procedures used in developing this model reflect this purpose. This report presents only the deflections along the vertical face between the aft dome and the nozzle fixed housing. Figure 4 shows a section of the aft dome/fixed

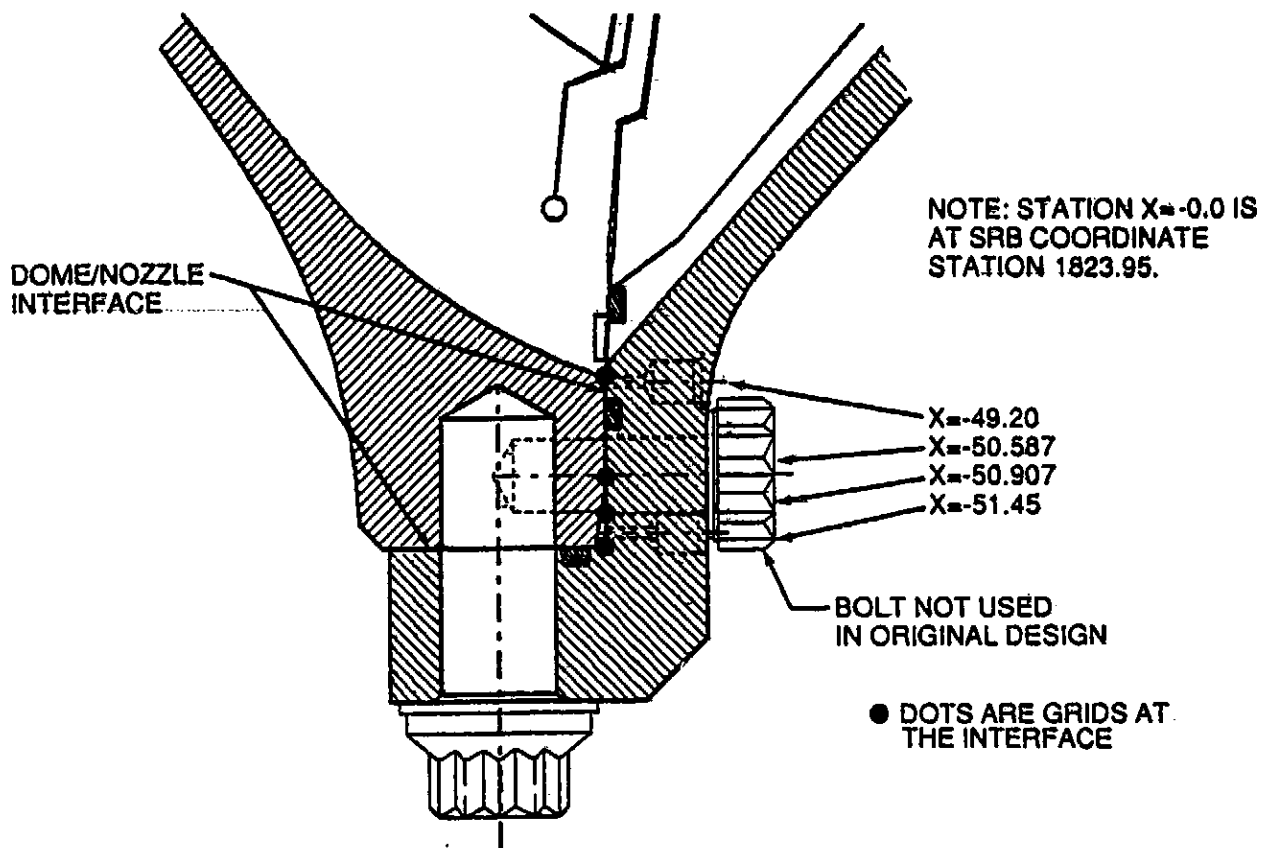


Figure 4. X-location of gridpoints in gap.

housing interface with these locations shown as dots where gridpoints were on this vertical face. For example, a dot (also a gridpoint), located at station -50.587 inches is at the centerline of the radial bolts.

III. THEORETICAL TREATMENT - ASSUMPTIONS AND EQUATIONS

The equations for this type of study primarily involve the use of large mass and stiffness matrices. The finite element technique, using NASTRAN for example, is a way of constructing the mass and stiffness matrices. These matrices are then used to develop a group of second-order differential equations which are to be solved simultaneously. The equations also include damping, which represents the structure's ability to absorb energy. Many types of loads are applied to the structure and are included in these equations. The equations, including mass, stiffness, damping, and applied forces, are as follows:

$$[M] \{\ddot{X}_i\} + [C] \{\dot{X}_i\} + [K] \{X_i\} = \{F_i\} \quad (1)$$

where

[M] – mass matrix

[C] – damping matrix

[K] – stiffness matrix

{F_i} – forces acting at grid i on the model

{X_i} – general vector representing the deflection at grid i on the model.

The mass matrix is an array representing the weight of the structure distributed over the grid points of the model, while the stiffness matrix is an array representing the stiffness between the grid points. The force vector on the right side of equation (1) are the forces acting at various grid points on the model. These forces include internal chamber pressure, blowout force, pressure forces and moments from nozzle gimbal, actuator gimbal forces, gravity, and quasi-static load factors. The pressure forces are applied in several different ways. The chamber pressure acts over the aft dome, the fixed housing, the nozzle, and other areas of the SRM. However, the math model in this report includes only the aft dome, fixed housing, and nozzle. The primary area of interest for this report is the worst case gap deflection at the aft dome to fixed housing interface around the entire 360 degrees of the model. The chamber pressure acting on the aft dome and fixed housing is applied as a force acting at each grid point. The pressures acting on the nozzle are integrated over the surface of the nozzle to establish forces and moments at the nozzle aft end ring face (Fig. 1). The gas dynamic equations used (from Reference 7) to establish the nozzle forces and moments were developed by the Morton Thiokol Space Division and are presented in the following for completeness.

The axial component (orbiter X-direction) of the force is:

$$F_{NBO} = A_n \cdot P_{chn} + T_{VAC} (1 - \cos \theta) + P_{Amb} (A_{EP} \cos \theta - A_{ER}) \quad (2)$$

where

F_{NBO} = nozzle axial blowout force – vertical component of gimbal nozzle force (parallel to motor axis), lb, _____

A_N = 1,026 in² – ratio of null position nozzle force to nozzle stagnation pressure,

P_{chn} = nozzle stagnation pressure, psia,

T_{VAC} = vacuum thrust, lb,

P_{Amb} = ambient pressure, psia,

A_{EP} = π(74.822)² = 17,588 in² – nozzle exit plane area,

$A_{ER} = \pi(39.22) = 4,832 \text{ in}^2$ -- area enclosed by aft end ring O-ring,

θ = gimbal angle, degrees.

The lateral component of the force (lb) due to gimbal angle is:

$$F_{NLat} = (T_{VAC} - A_{EP} P_{Amb}) \sin \theta \quad (3)$$

The force direction is opposite to that of the gimbal direction.

The yaw/pitch moment (in-lb) at the aft end ring due to nozzle gimbal is:

$$M_{Y/PB} = Z_{PP} F_{NLat} \quad (4)$$

where

$Z_{PP} = 6.057 \text{ in}$ = moment arm between nozzle pivot point and aft end ring face.

The lateral component of the transient force (lb) due to gimbaling rate is:

$$F_{NLatTr} = (4.521 \times 10^{-5}) L_N \dot{m} \dot{\theta} \cos \theta \quad (5)$$

where

$L_N = 175.757 \text{ in}$ = nozzle nose to exit length,

$\dot{\theta} = 5 \text{ deg/s}$ = maximum nozzle gimbaling rate,

\dot{m} = total mass flow rate, lbm/s.

The axial component of the transient force due to gimbaling rate is:

$$F_{NBOTr} = (4.521 \times 10^{-5}) L_N \dot{m} \dot{\theta} \sin \theta \quad (6)$$

The transient yaw/pitch moment at the aft end ring face due to gimbaling rate is:

$$M_{Y/PTr} = (4.521 \times 10^{-5}) Z_N L_N \dot{m} \dot{\theta} \quad (7)$$

where

$Z_N = 53.221$ in = moment arm between nozzle midpoint and aft end ring face.

Equations (2) through (7) give the forces caused by the gas dynamics involved while operating the SRM. These forces, as described, act at the nozzle aft end ring face with the associated moments. Equation (2) gives the nozzle blowout force which acts in the direction of the Space Shuttle Vehicle (SSV) X-axis on the nozzle and tends to push the nozzle downward, (i.e., the SSV + X direction). Equation (3) gives the lateral force acting on the nozzle caused by thrust and nozzle gimbal. Equation (4) gives the moment acting on the aft end ring face with the force $F_{NL,at}$ also applied at the aft end ring face. Equations (5), (6), and (7) give forces caused by the nozzle gimbal rate and the fact that there is a fluid mass moving through the nozzle. These forces and moments, in most cases, are going to be small and will have little influence on the gap motion studied in this analysis, compared to the effect of the internal chamber pressure and the radial bolt preloads which have more influence.

Now that the various parts of equation (1) have been described, the solutions to this equation and their uses will be discussed. The direct transient response analysis, the static analysis, and the base driving response analysis were all solved using different techniques which will be discussed in the following paragraphs.

A. Direct Transient Response Analysis

The direct transient response approach was used to calculate vibrational motion of the gap caused by the buildup of the SRM chamber pressure at ignition and gimbal forces (caused by the nozzle). This approach is referred to as a direct approach because equation (1) is used in NASTRAN and solved without calculating modes and frequencies of the model. In other words, the modal response method was not used. The equation was solved numerically in NASTRAN (i.e., not in closed form). The input forces build up from zero to their maximum values using the same time scale and shape of curve as the chamber pressure rise curve. The loads applied were the internal chamber pressure, the nozzle blowout force, and the side forces and moments from nozzle gimbal as shown in equations (2) through (7). The chamber pressure is distributed over the aft dome and fixed housing while the blowout force is acting on the top end of the nozzle and the gimbal side forces are applied at the nozzle aft end ring face. The results of this study are presented in Section V.

B. Static Analysis

The forces used in the static analysis were the maximum forces from the direct transient response analysis while also including the nozzle actuator forces and the liftoff load factors. The static analysis was also conducted using NASTRAN. The stiffness matrix of the math model was used to obtain deflections and stresses. The mass matrix was also used in the analysis to apply the liftoff load factors at each grid point of the model to establish the acceleration induced loads. The nozzle actuator forces were applied to the nozzle at the locations where the bottom of the actuator ties into the nozzle. These forces were calculated using the maximum nozzle design bending moment of 4,210,000 in-lbs (obtained from Reference 8).

C. Base Driving Response Analysis

The base driving-response approach was used to determine the influence that vehicle dynamic motion (vibration) has on the gap deflections at the aft dome to fixed housing interface. The vehicle dynamic accelerations were taken from Rockwell loads studies performed on the entire shuttle vehicle (launch configuration). The accelerations were defined in these studies at four positions around the case at SRB station 1,606.72 in, 90 degrees apart in the SSV coordinate system Y-Z plane. The math model has its boundaries at station 1,823.95 in. Therefore, one of the assumptions for this analysis was that the accelerations at the two SRB stations would be similar in both magnitude and frequency content. These accelerations were available at these points around both the left and right-SRB's. The worst case accelerations were obtained from these data in each of the three directions and placed at all 50 boundary points around the model to perform the base drive analysis. The equation used to perform this operation is derived in the Appendix as equation (26) and is presented here as equation (8).

$$[M_{eq}] \{\ddot{q}\} + [2\zeta\omega] [M_{eq}] \{\dot{q}\} + [\omega^2] [M_{eq}] \{q\} = [\phi]^T (\{F_2\} - [M_{21}] \{\ddot{X}_1\} - [M_{22}] [\beta] \{\ddot{X}_1\}) \quad (8)$$

where

$$[M_{eq}] = [\phi]^T [M_{22}] [\phi] \text{ (generalized mass)}$$

$$[2\zeta\omega][M_{eq}] = [\phi]^T [C_{22}] [\phi] \text{ (generalized damping)}$$

$$[\omega^2][M_{eq}] = [\phi]^T [K_{22}] [\phi] \text{ (generalized stiffness)}$$

and,

$$[M_{22}] = [M] \text{ ---}$$

$$[C_{22}] \equiv [C]$$

$$[K_{22}] = [K]$$

are from equation (1) of this section.

The other variables are

$\{\ddot{X}_1\}$ - boundary base driving accelerations,

$\{F_2\}$ - applied forcing functions = $\{0\}$ for base driving,

$[\beta]$ - rigid body transformation that changes boundary accelerations to body (model gridpoint accelerations),

$[M_{21}]$ - partition of mass matrix related to the ground points; only appears in the free-free partition of the matrix,

$\{q\}$ - generalized modal coordinates,

$[\phi]$ - the modal deflections calculated from equation (1).

The flow chart for the computer program which runs this analysis is diagrammed in Figure 5. The program resides on computer files and is run using FORTRAN programs. The chart begins on the left with data on file created using NASTRAN and other FORTRAN programs. The chart ends on the right with response versus time of accelerations and deflections. It can be seen that the final deflections versus time in physical discrete coordinates are calculated from the following equation:

$$\{X_2(t)\} = [\beta] \{X\} + [\phi] \{q\} \quad (9)$$

where X is the motion at the support points of the hardware and q is the vibrational motion of the point in generalized coordinates. The product of $[\phi]$ and $\{q\}$ transforms the deflections into physical discrete coordinates represented by $X_2(t)$.

IV. TYPES OF ANALYSES

A. Modal Analysis

The modal analysis was conducted on the aft case/fixed housing model with the nozzle beam model to obtain the modes, frequencies, and the mass and stiffness matrices for use in the base driving response analyses.

A detailed math model of the aft case to fixed housing was developed to ensure a high degree of fidelity at the joint, but the nozzle was represented by a beam model developed with a minimum number of DOF. However, to ensure accurate results, the nozzle beam model was tuned to match results of a very detailed modal analysis of a cantilevered nozzle, which included steps of tuning the model without the actuators, and then with them attached. This detailed analysis is published in References 5 and 6.

The SRB mass property document was also used to obtain the correct mass for both the detailed part of the model and the simplified nozzle part of the model as well as the total mass for the combined model. The masses from this analysis compared well with the masses found in the mass property report. The frequencies and mode shape descriptions of this model are shown in Table 1 and the mode shapes are plotted in Figures 6 through 12. The lower frequency modes describe motion of the nozzle which is represented by beams and are seen as lines coming out of the bottom center of the model on the views shown of the modal plots. Modes 6 and 7 involve most of the flexible motion of the entire aft dome and fixed housing.

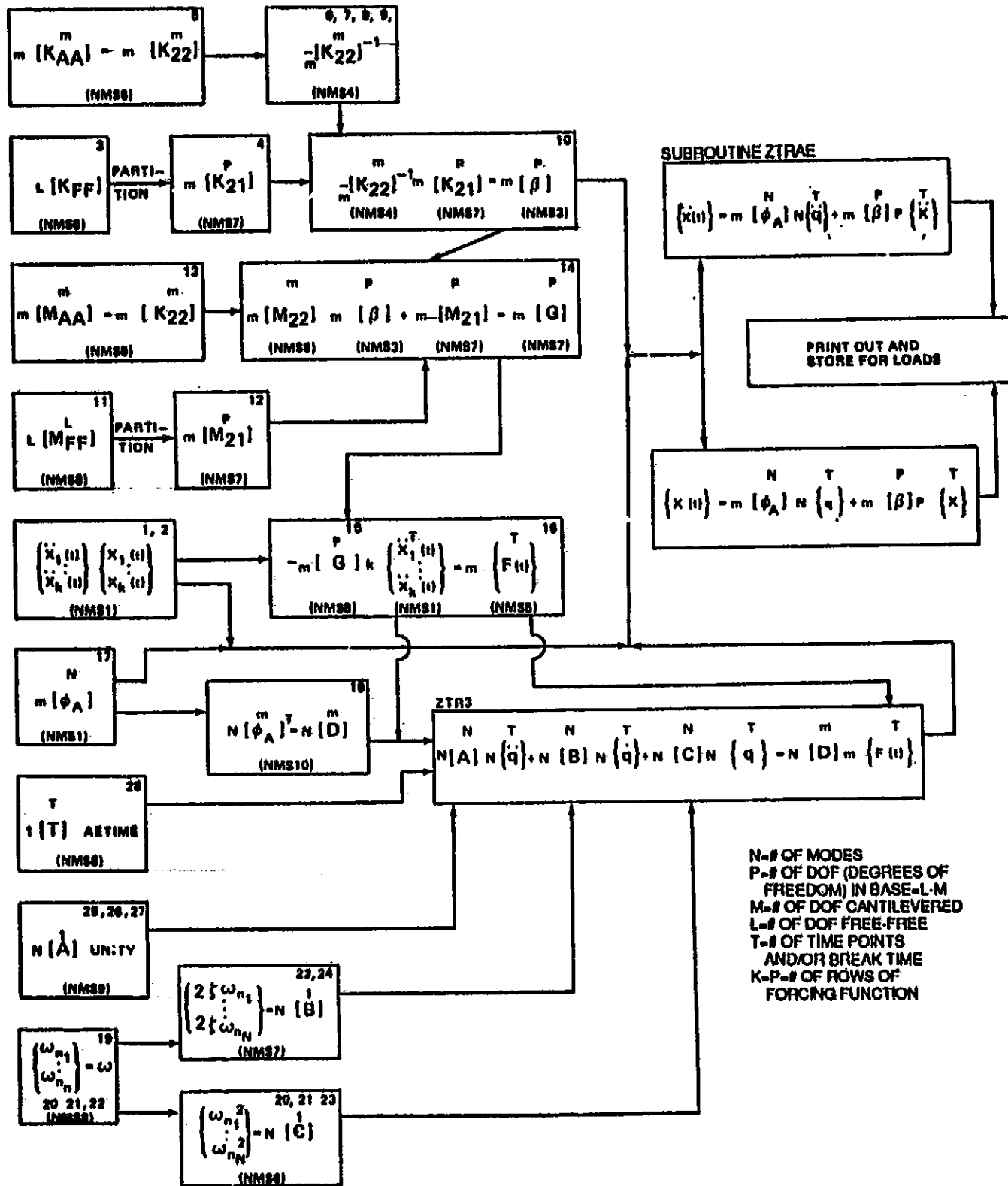


Figure 5. Base driving analysis flow chart.

TABLE 1. FREQUENCIES AND-MODE SHAPE DESCRIPTIONS

Mode	Frequency	Description
1	2.22Hz	First torsional mode of nozzle.
2	14.73 Hz	First vectoring mode of nozzle
3	15.27 Hz	Second vectoring mode of nozzle.
4	22.28 Hz	Third vectoring mode of nozzle
5	22.32 Hz	Fourth vectoring mode of nozzle.
6	65.47 Hz	Vectoring mode of nozzle combined with flexing of dome
7	185.5 Hz	Flexing mode of dome combined with much dome torsion

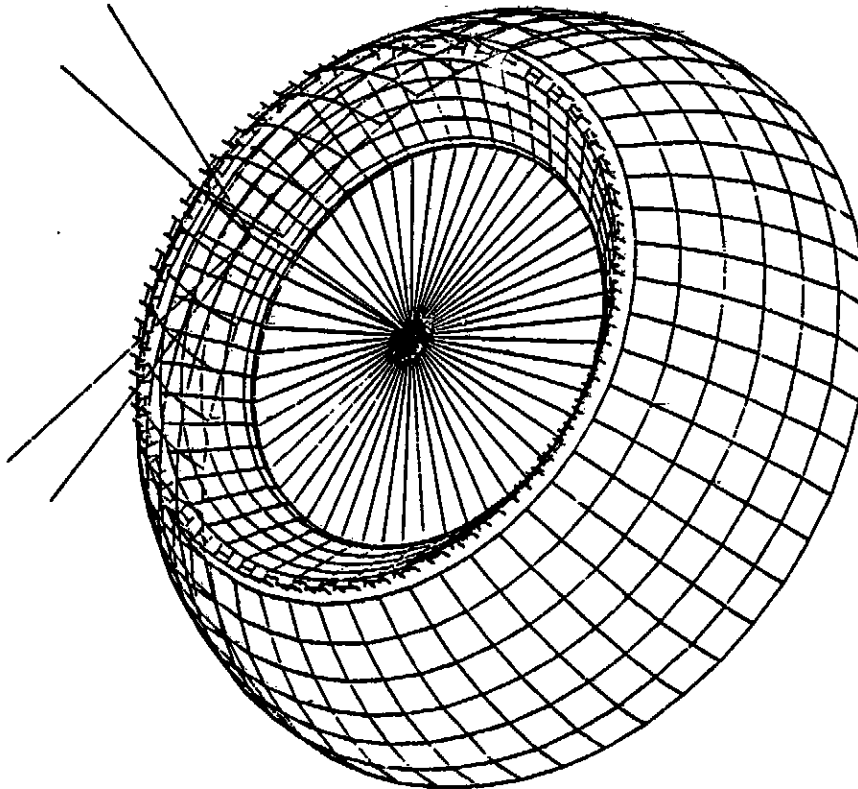


Figure 6. Modal deformation: Mode 1, frequency 2.22 Hz.

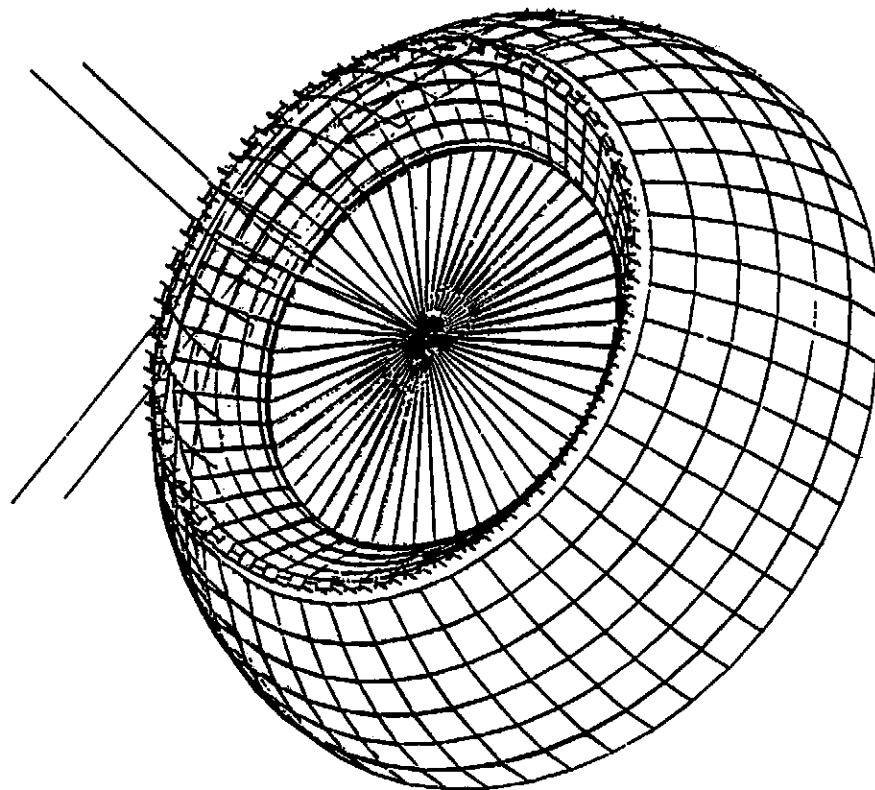


Figure 7. Modal deformation: Mode 2, frequency 14.73 Hz.

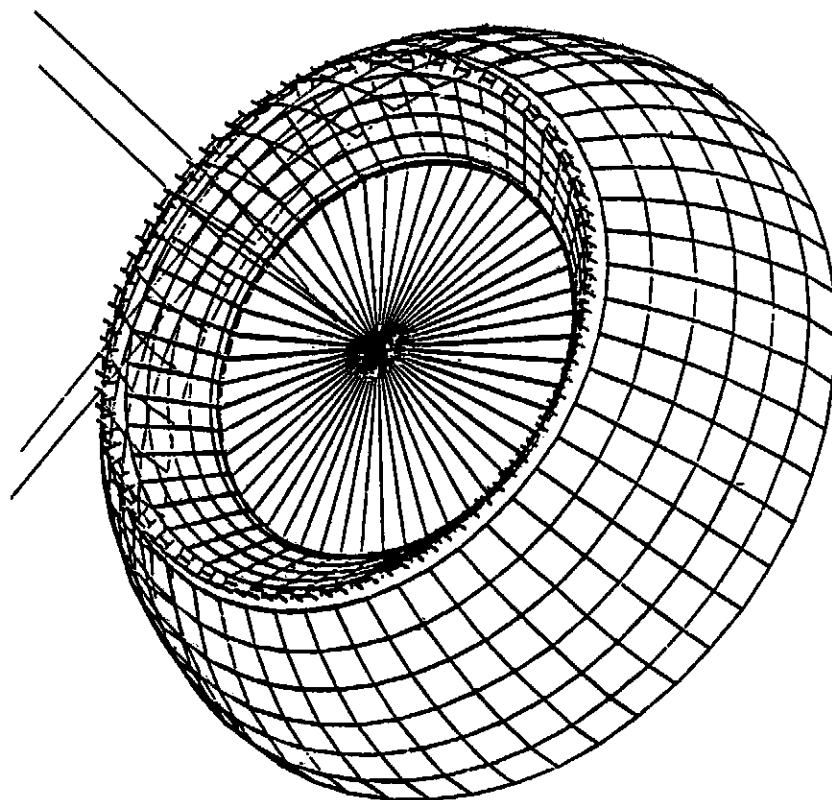


Figure 8. Modal deformation: Mode 3, frequency 15.27 Hz.

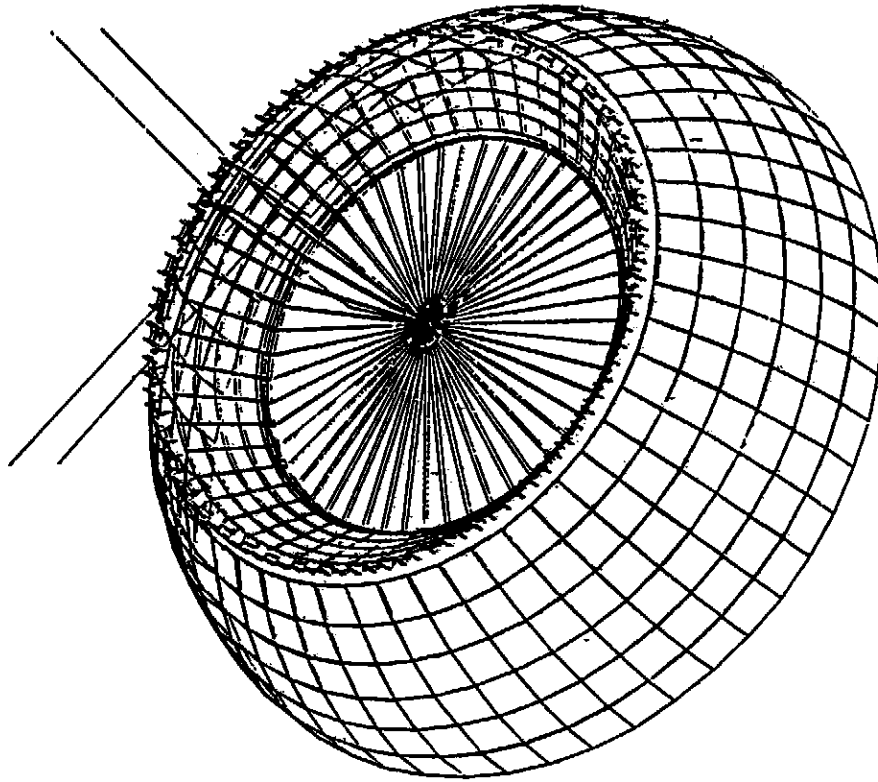


Figure 9. Modal deformation: Mode 4, frequency 22.28 Hz.

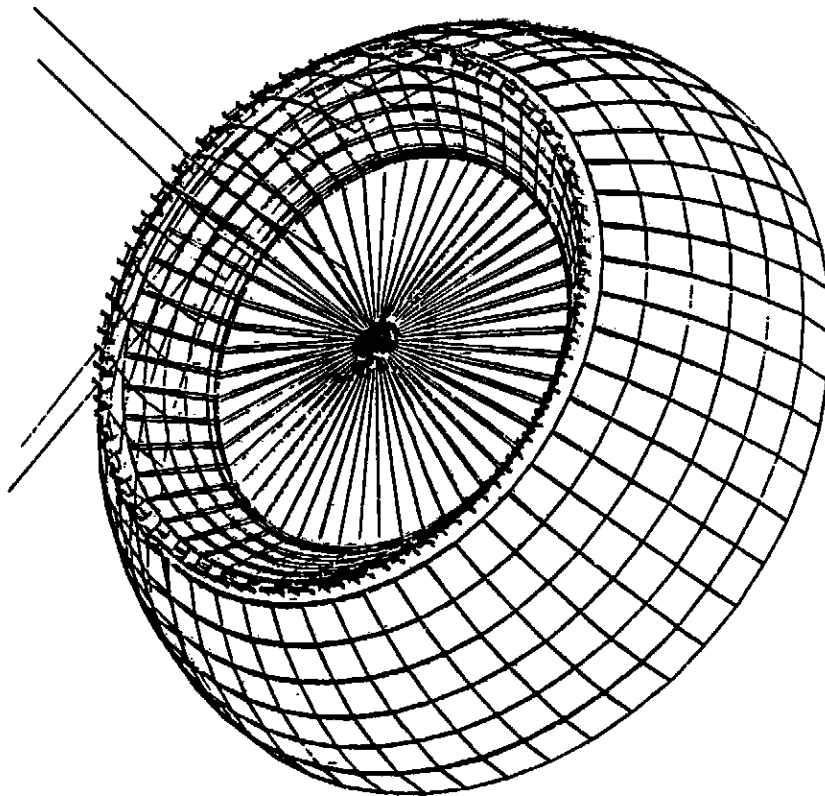


Figure 10. Modal deformation: Mode 5, frequency 22.32 Hz.

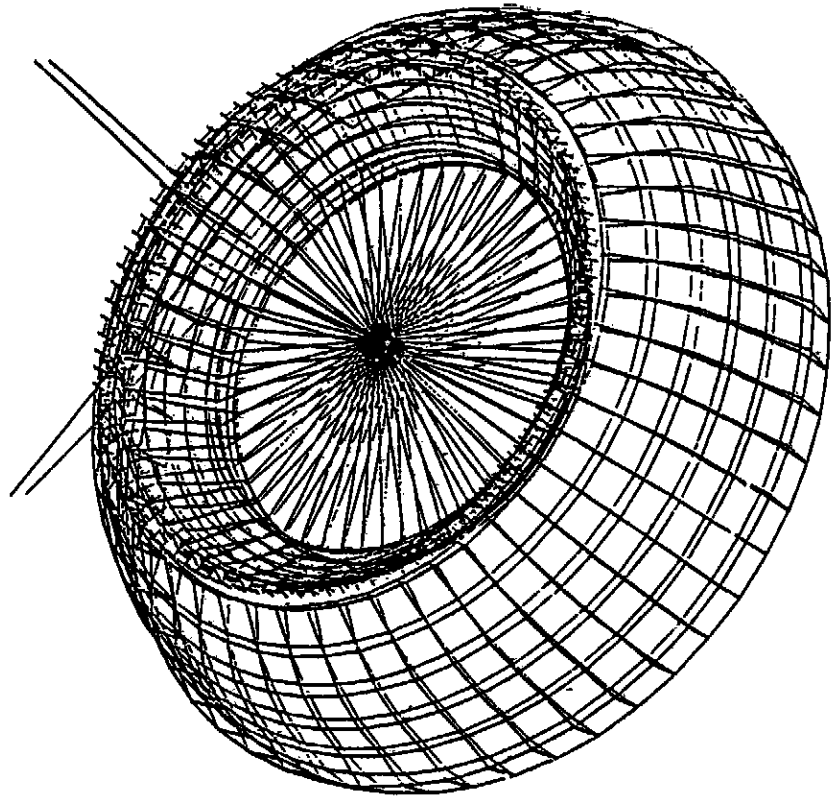


Figure 11. Modal deformation: Mode 6, frequency 65.47 Hz.

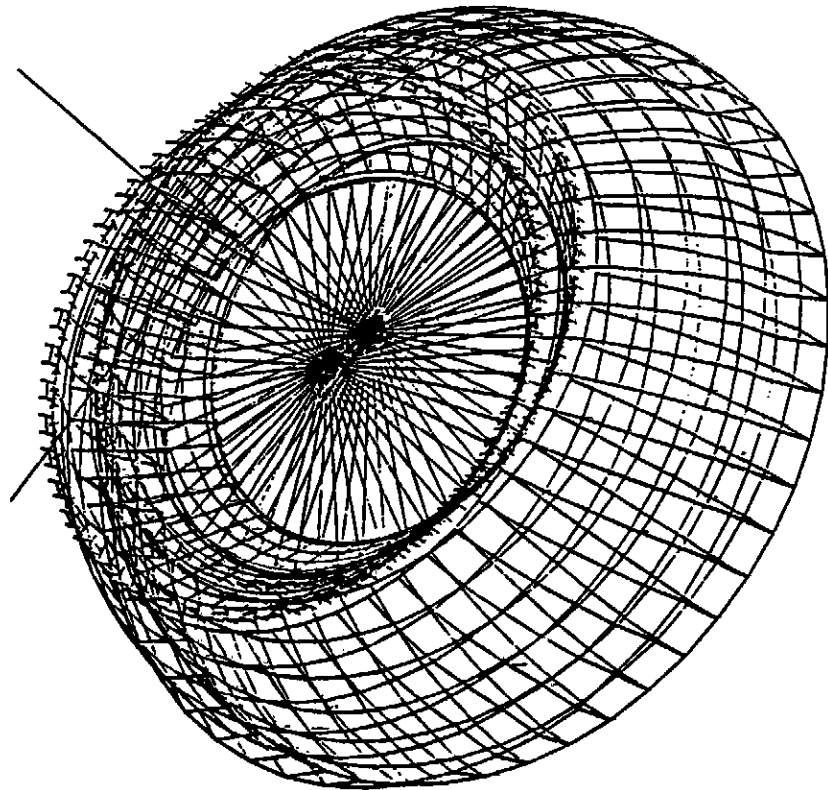


Figure 12. Modal deformation: Mode 7, frequency 185.5 Hz.

B. Static Analysis

The static analysis involved applying the maximums for every type of load considered. The loads applied were internal chamber pressure, nozzle blowout forces, actuator gimbal forces, vertical and radial bolt preloads, gravity magnified by a steady state acceleration factor, and vehicle low frequency vehicle dynamic accelerations applied at all the grid points in the model. This was done for each flight event, a total of five different subcases (flight times). Each flight event involved a subset of these forces using the applicable values for the maximum in each subcase.

The first event considered, liftoff, was the only case in which the vehicle low frequency vehicle dynamic accelerations (quasi-static) were applied. The other four events – roll maneuver, maximum dynamic pressure (max q), maximum acceleration (max g), and pre-staging (SRB separation) – include the remainder of the loads considered. A table summarizing these values used in each of the five cases is shown in Table 2.

In addition to all these cases, the model was run without the radial bolts, as in the old design, to compare the behavior of the no-bolt configuration to that of the new 7/8-in radial bolt flight configuration. The force values used in the no-bolt analysis are also the ones shown in Table 2.

C. Transient Response Analysis

In the transient response analysis, the opening of the gap was computed as a response to the input pressure transient (Fig. 13) and other forces related to the pressure transient such as the blowout forces. This analysis was performed to observe the dynamic effects (overshoot, amplification, etc.) on the gap opening compared to the static value of the gap opening. For this reason, the slope of the chamber pressure rise curve is important. For example, if the chamber pressure curve rises to a peak from zero time to a time equal to one-fourth the period of the first natural frequency of the structure, then large vibrational responses in the structure can occur.

An enveloping pressure curve was obtained from References 9 and 10 and used to force the math model. The curve is a smooth pressure rise curve with the dynamic behavior of the model mainly sensitive to the slope of the curve. The pressure rise curve builds up in 0.2 s. This would resonate with a frequency of approximately 1 Hz, $1/(4 \times 0.2) = 1.25$ Hz. The lower frequencies of the whole model with the nozzle are 14 Hz to 22 Hz and the natural frequency of the aft dome/ fixed housing is 65 Hz. It can be seen by comparing these frequencies to the forcing function frequency that there will probably be very little dynamic response due to the pressure transient curve.

A check case was run with the slope of the pressure transient curve increased by a factor of 10. The results show an increase in the amount of the dynamic response, but compared to the static part of the deflection, the dynamic portion of the deflection is still very small. These response plots are shown in Section V.

TABLE 2. SUMMARY OF FLIGHT LOADS

	Liftoff	Roll Maneuver	Max Q	Max G	Pre-Stage
Internal pressure	920 psi	930 psi	788 psi	673 psi	90.7 psi
Steady state acceleration (G's)	1.4	1.4	2.0	3.0	3.0
Blowout forces:					
Axial (lb)	1.13 + 6	1.14 + 6	8.60 + 5	7.07 + 5	9.30 + 4
Side (lb)	113,649	285,261	265,833	171,362	43,609
Moment (in-lb)	24,653	25,616	21,923	19,157	2,960
Actuator loads:					
X	23,320	23,320	23,320	23,320	23,320
Y	-51,621	-51,621	-51,621	-51,621	-51,621
Quasi-static load factors:*					
X	+ 1.0/-4.0				
Y	± 1.6				
Z	± 6.8				
(Nozzle mass = 18,873 lb)					

*From Reference 8.

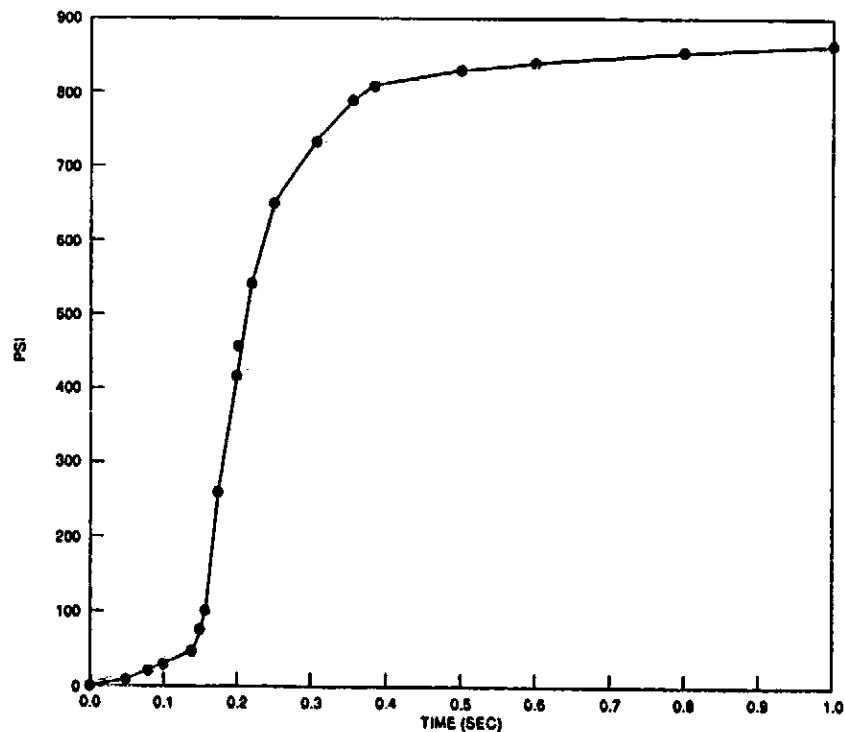


Figure 13. Measured pressure on aft SRM dome.

D. Base Driving Response Analysis

The base driving response analysis was conducted using the model analysis data described above in Section IV.A. Vehicle acceleration time histories from coupled loads analysis were used at the model attach points to drive the model. Typical plots of these time histories at a grid are shown on Figures 14, 15, and 16.

The flow chart (Fig. 5) shows all the steps necessary to calculate loads and deflections from base input accelerations. Steps 1 and 2 (step numbers are shown in the upper right corners of the blocks), show the accelerations and enforced displacements used to drive the model as input to start the analysis. Steps 3 through 14 show all the matrix manipulations performed using the mass and stiffness matrices. Both the free-free matrices, M_{ff} and K_{ff} , were input to the base driving program and disassembled into the ground motion partitions, M_{21} and K_{21} , and the cantilevered partitions, M_{22} and K_{22} . It is also possible to obtain these cantilevered matrices directly from a modal analysis with the base of the model constrained. To make the partitioning step a single operation, the ground points in both matrices were repositioned to the first rows (and columns) while using NASTRAN. The K_{22} partition of the stiffness matrix was inverted and combined with the other partition of the stiffness matrix to form a new matrix called the beta (β) matrix. This new matrix is then combined with the M_{22} partition and added to the M_{21} partition of the mass matrix to form a coefficient matrix for the base input accelerations. This coefficient was developed in equation (8) of the previous theoretical section.

The mode shapes, natural frequencies, normalized mass matrix, and the time vector (steps 15 through 27), along with the newly formed forcing function matrix, are then fed into a modal response subroutine shown in Figure 5 as ZTR3. The modal responses from the ZTR3 routine are then used as input for another response subroutine (ZTRAE) where these responses are transformed back into physical domain accelerations, velocities, and deflections. These physical coordinates describe the model's response to the original input forcing functions giving the gap deflections and loads as desired. The results of this analysis are shown in Section V.

V. RESULTS

A. Model Verification with Transient Pressure Test Article (TPTA) Test Results

The TPTA test series were used to verify the aft case/nozzle joint model for these analyses by using the math model with slight changes in its configuration to model TPTA conditions accurately. Details of the TPTA test setup were obtained from Reference 11. The TPTA test used loads matching the flight values except for bolt preloads and nozzle loads. The test also had slightly different boundary conditions. The actual test set-up had a plug fitted tightly into the fixed housing/nozzle interface area with an O-ring sealing this joint for the TPTA test.

The main modification to the math model was removing the beam model of the nozzle and fixing the boundary conditions at the fixed housing/plug interface in all translational directions except the X-direction. This, most likely, makes the model stiffer than the test article in this area. Other modifications included lowering the radial and vertical bolt preloads from the flight values to

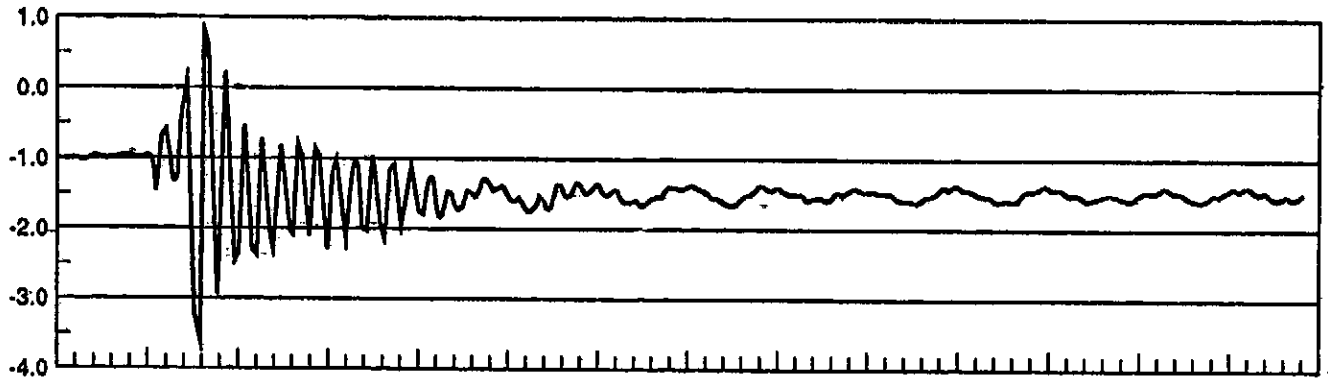


Figure 14. Base driving forcing function X-direction.

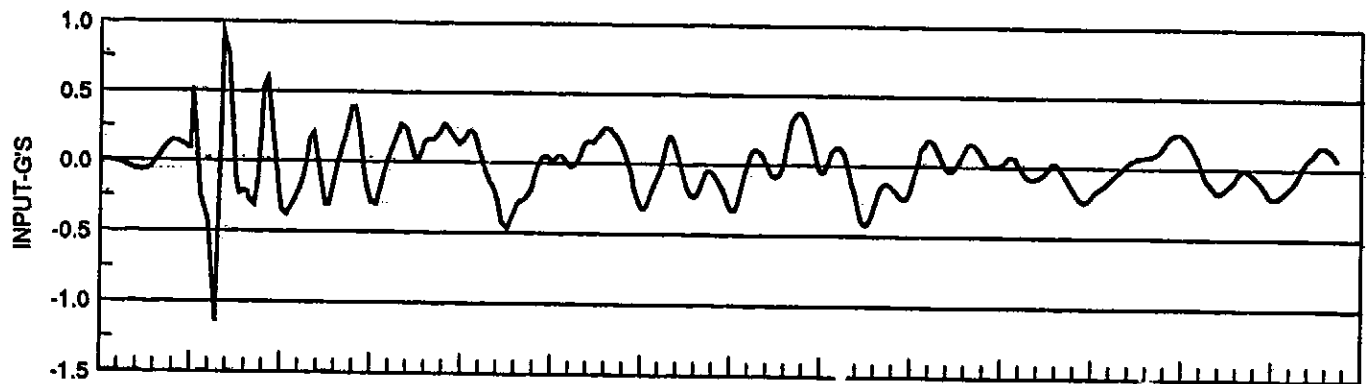


Figure 15. Base driving forcing function Y-direction.

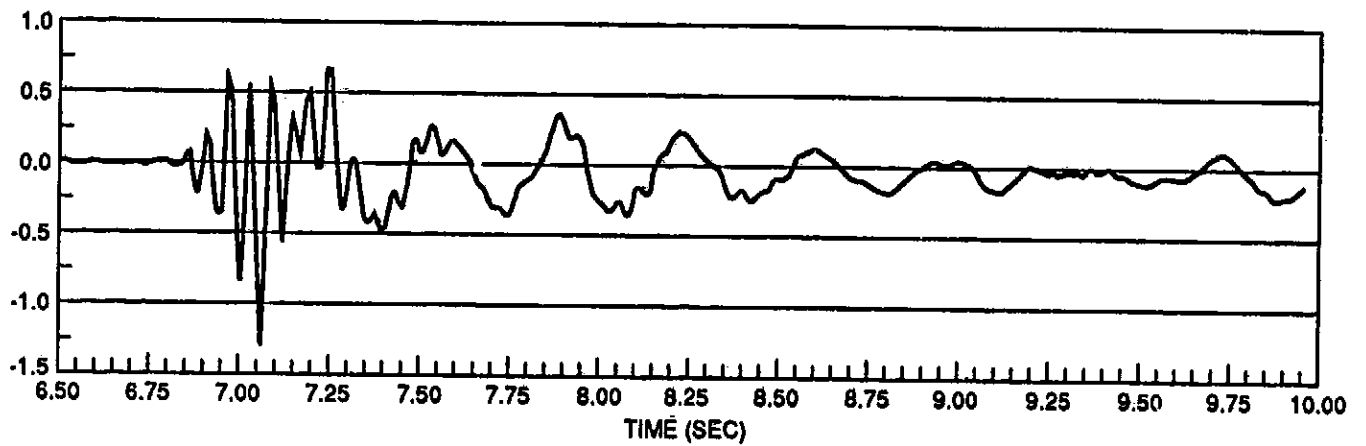


Figure 16. Base driving forcing function Z-direction.

the test values. Typical preload values for the flight configuration for the vertical and radial bolts are 141,000 and 45,000 lb, respectively. The preloads for the TPTA tests compare at 92,000 and 25,000 lb for the vertical and radial bolts.

The deflection gauge locations used in the TPTA test were at the same circumferential locations as the model where grid points and displacement information was retained. These locations were obtained from Morton Thiokol drawing No. 7U75234 [12].

The plot in Figure 17 shows the individual data points from the first TPTA test as stars and the analytical results from the model as circles connected with a line. The two sets of data are plotted together to show the similarity between the test results and the analysis results. The analytical results envelope the test data which shows that the model is conservative for studying the joint behavior.

B. Analyses Results

Results of the static and dynamic deflection analyses for the flight configuration are covered in this section. In general, the maximum envelope results of all cases are shown. Four locations with grid points were used in the model on the vertical face at the aft case/fixed housing interface shown in Figure 4. The results for the vertical face are summarized on Figures 18 through 22. The actual deformations calculated by the model along the vertical face are shown as deflected shapes.

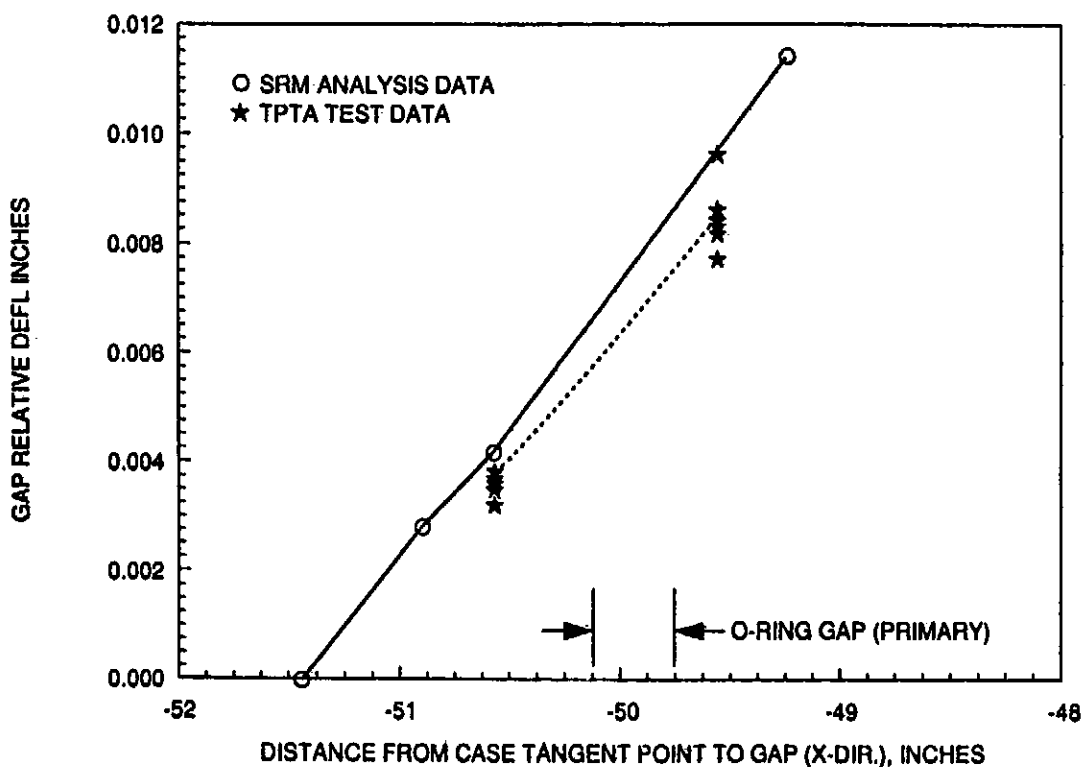


Figure 17. Static gap between fixed housing and aft dome - TPTA test.

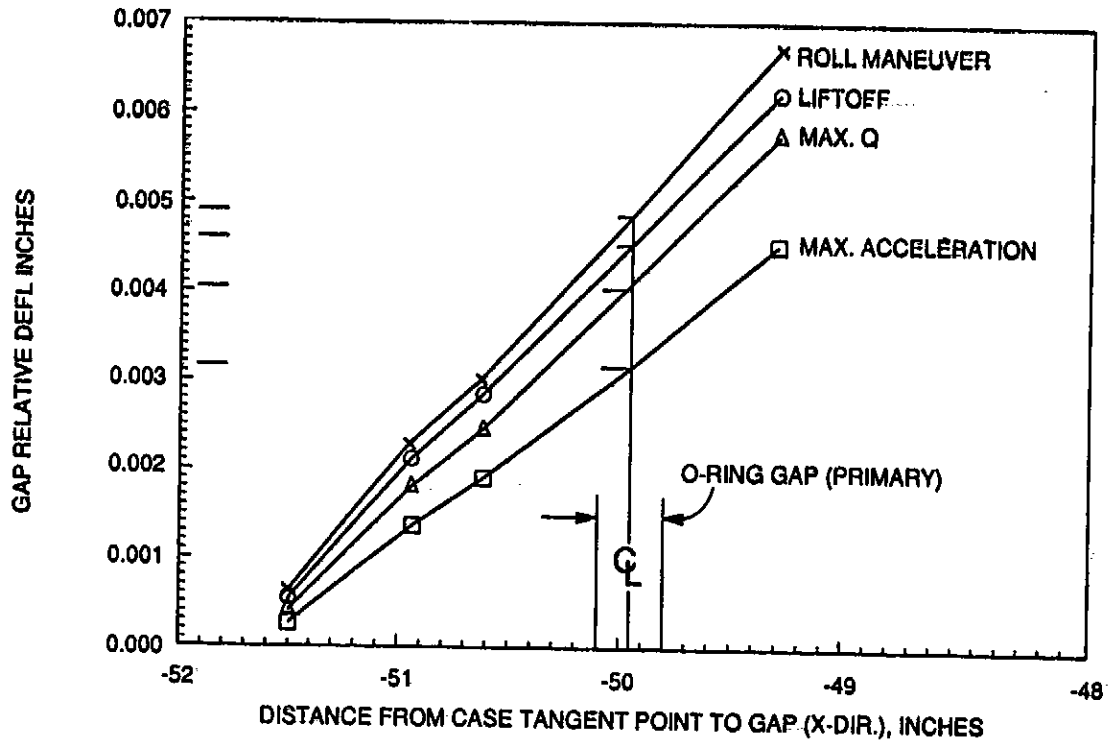


Figure 18. Static gap between fixed housing and aft dome – flight math model.

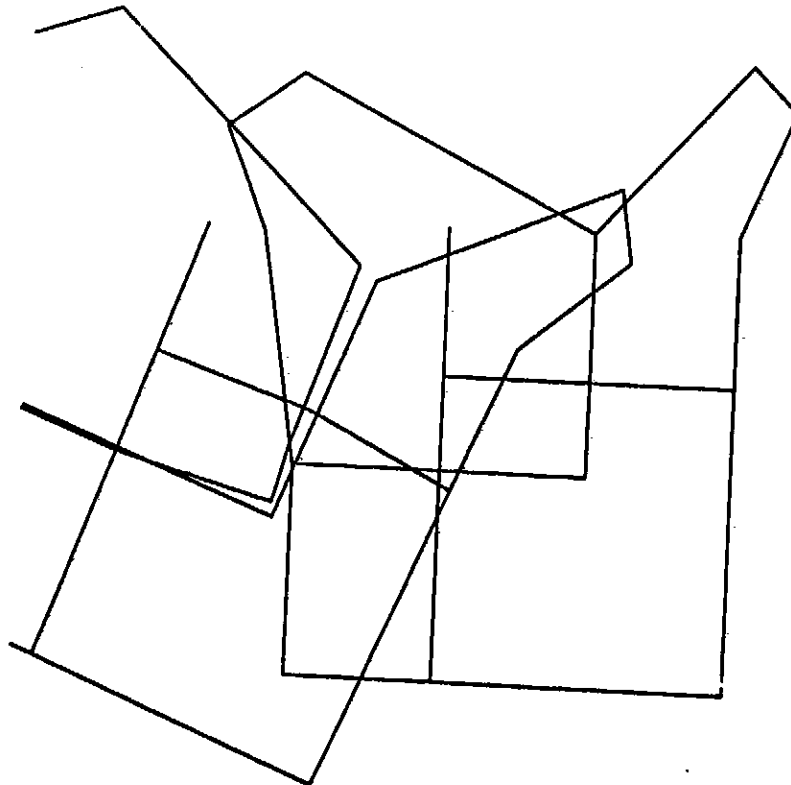


Figure 19. Static deflected model compared with undeflected model.

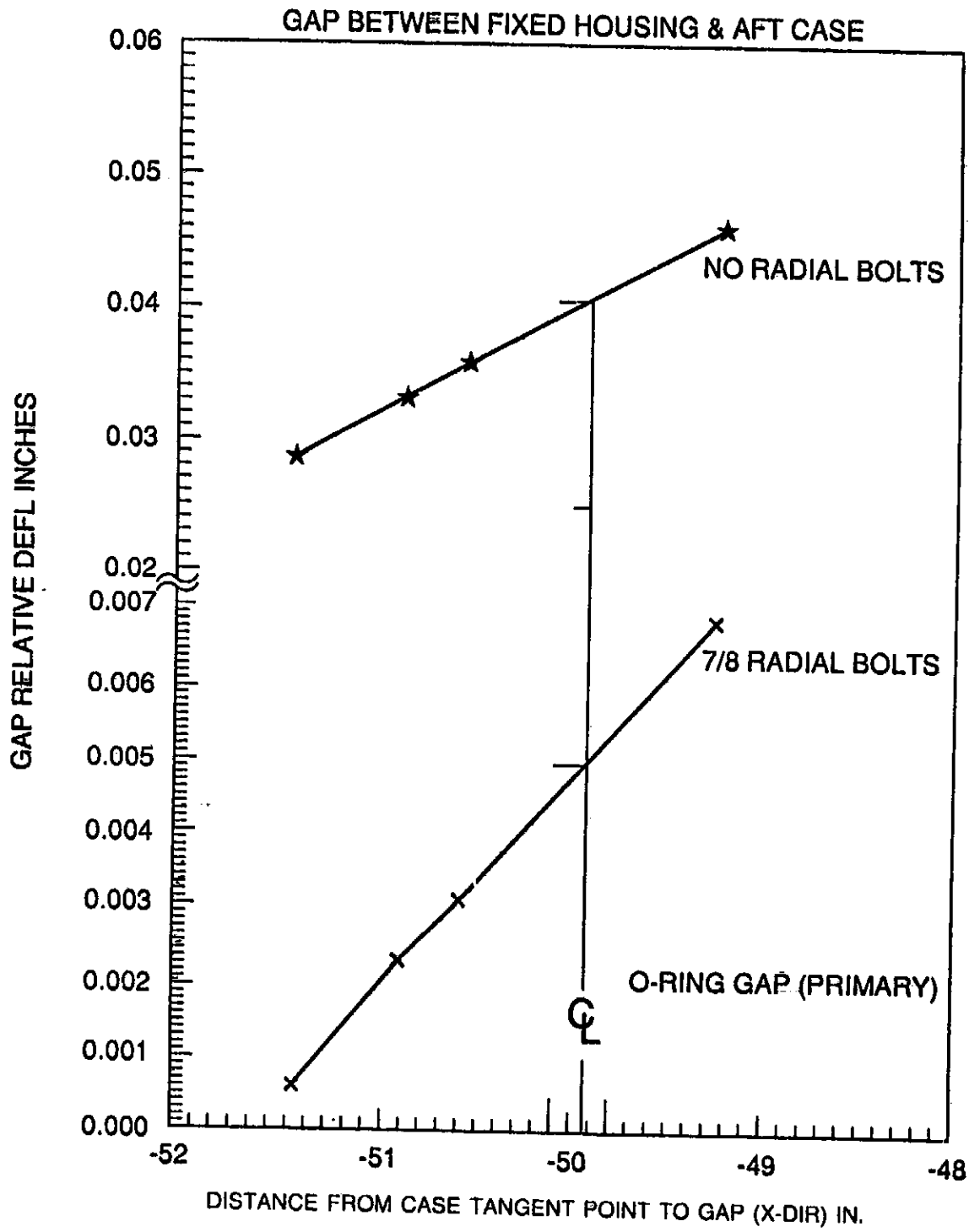
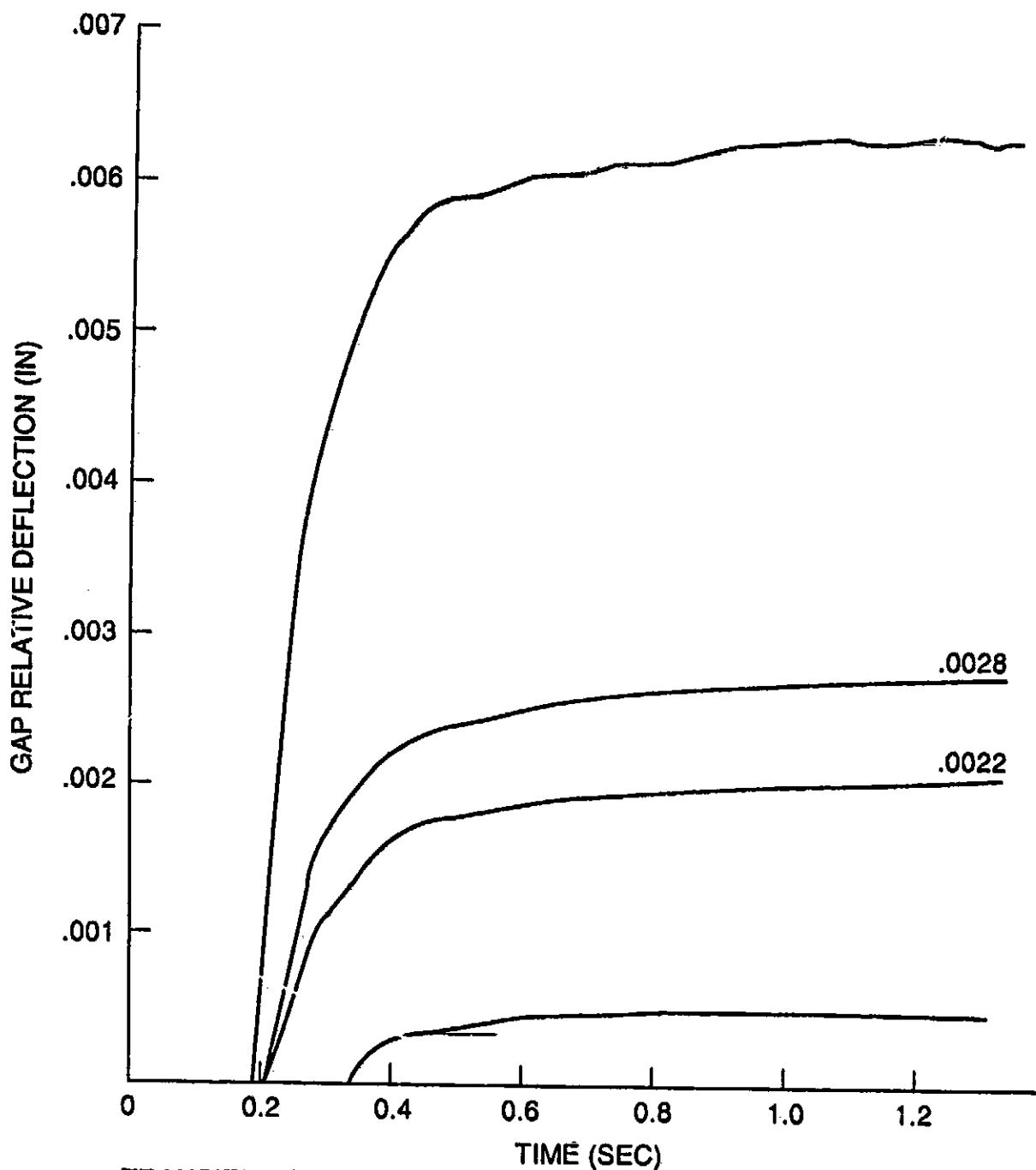


Figure 20. Gap deflections with and without radial bolts.



TRANSIENT ANALYSIS NOZZLE/CASE (FIXED)
 MODELED WITH UPDATED BLOWOUT AND
 GIMBAL FORCE ANALYZED TO GET RELATIVE
 GAP DEFLECTIONS

Figure 21. Transient analysis gap deflections.

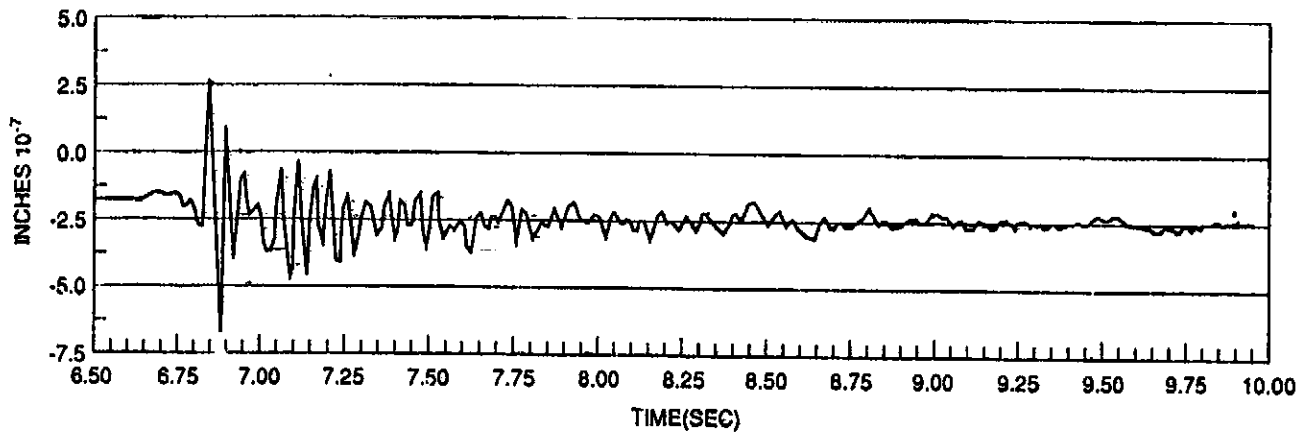


Figure 22. Relative vibration gap motion at aft dome/fixed housing (X-direction).

on Figure 18. Figure 18 shows the deflections at different flight events plotted to scale, while Figure 19 gives the cross-section deflections amplified by a large scale factor so that the general shape of the deflection pattern can be studied.

Figure 20 shows two static deflection curves, in the radial direction, for the vertical part of the gap between the aft case dome and the nozzle fixed housing for 930 psi chamber pressure and 4.8-degree nozzle gimbal angle. Curves are shown for the configuration without radial bolts (old design) and with the 7/8-inch radial bolts (new design). Deflections at the centerline of the primary O-ring gap can be seen by following the horizontal axis to the markings on the graph and going up to both curves. The left end of each curve is the bottom of the vertical part of the gap between the aft case and the fixed housing and the right end is the top. As can be seen from the figure, the 7/8-inch radial bolt reduces the gap opening by almost an order of magnitude with respect to the configuration without radial bolts. Figure 18 shows the results of the studies using the 7/8-inch radial bolts for different flight times and conditions (chamber pressure and nozzle gimbal angles). The top curve is for the vehicle roll maneuver case. This case was run using 930 psi as the motor internal chamber pressure, a nozzle gimbal angle of 4.8 degrees, with blowout forces, actuator forces, steady-state vehicle accelerations, gimbal side force and moment. The next worst case is liftoff, with 920 psi chamber pressure, 2-degree nozzle gimbal angle, liftoff vehicle accelerations, and the same type of forces and moments as indicated above for the roll maneuver. The third curve is for the maximum dynamic pressure event with parameters of 788 psi chamber pressure and 5-degree gimbal angle. The last case shown is for the maximum acceleration case using 673 psi and 3.7-degree gimbal angle.

Transient response results during liftoff are shown as gap relative deflection versus time on Figure 21. The four curves are the four locations on the vertical face where the relative deflections were calculated as shown on Figure 4. These curves follow the shape of the pressure versus time with only a slight amount of vibration as shown on the curves in the period of time when the maximum pressure is reached. These curves are presented to show the small amount of vibration which occurs in the gap between the aft dome housing and nozzle fixed housing as a result of the applied transient forces. The maximum deflection at the top of the gap is 0.0063 inch as shown.

Studies were also performed using liftoff vehicle dynamic motion base drive the nozzle/aft case joint structural model with acceleration time histories from STS coupled loads analysis [13]. The results of this study show extremely small deflections at the nozzle/aft case joint gap as a

result of vehicle low frequency vibration input. This can be seen on Figure 22 and shows the relative deflection between both sides at the top of the gap. As can be seen, the relative deflections are very small compared to the other analyses (of order $< 1 \times 10^{-6}$). Other deflections down the face of the vertical part of the gap will be smaller.

These analyses have shown that nozzle-to-case joint dynamic gap deflection motion caused by SRB internal chamber pressure buildup, nozzle gimbaling, and vehicle low frequency dynamic motion is very small compared to the static gap deflection. The maximum gap opening at the centerline of the primary O-ring is approximately 0.0049 inch using the 7/8-inch radial bolt configuration with a nominal preload of 45,000 lb.

VI. CONCLUSIONS AND RECOMMENDATIONS

A very large finite element analytical math model of the SRM aft dome/nozzle joint for the Space Shuttle vehicle was developed to investigate gap deflections at the O-ring seal during simulated flight operation. All in-flight static and dynamic environments or forcing functions were applied to the analytical model to calculate the gap deflections. In addition, the finite element math model was modified slightly to simulate an experimental program conducted to measure the gap deflections. The analytical and experimental results closely match. This comparison provides confidence in analytically predicting the gap deflections during flight, and is considered a step forward in the use of finite element modeling techniques for large complex structures. It is recommended that this type study be conducted in the future on all O-ring interfaces for high pressure solid rocket motors.

APPENDIX

Response Equations for Base Motion Excitation

By Wayne Holland, S&E-ASTN-ADL

March 1, 1971

The equation of motion for a discretely modeled structure can be written in matrix form as

$$[M] \{\ddot{X}\} + [C] \{\dot{X}\} + [K] \{X\} = \{F(t)\} \quad (1)$$

where:

$[M]$, $[C]$, $[K]$ = mass, damping, and stiffness matrices, respectively

$\{\ddot{X}\}$, $\{\dot{X}\}$, $\{X\}$ = acceleration, velocity, and displacement vectors of discrete coordinates.

Consider that the system of equation (1) has n number of degrees of freedom. That is $[M]$, $[C]$, and $[K]$ are $n \times n$ matrices and, correspondingly, $\{\ddot{X}\}$, $\{\dot{X}\}$, $\{X\}$, and $\{F\}$ are $n \times 1$ matrices (vectors). Additionally, consider that m number of the displacements are known or prescribed. The known or prescribed displacement functions are referred to as base motions.

We can partition equation (1) to reflect the prescribed coordinates in the $m \times 1$ vector, $\{X_1\}$, and the remaining coordinates in the $(n-m) \times 1$ vector, $\{X_2\}$. With this partitioning scheme, equation (1) takes the form

$$\begin{bmatrix} M_{11} & M_{12} \\ \text{---} & \text{---} \\ M_{21} & M_{22} \end{bmatrix} \begin{Bmatrix} \ddot{X}_1 \\ \text{---} \\ \ddot{X}_2 \end{Bmatrix} + \begin{bmatrix} C_{11} & C_{12} \\ \text{---} & \text{---} \\ C_{21} & C_{22} \end{bmatrix} \begin{Bmatrix} \dot{X}_1 \\ \text{---} \\ \dot{X}_2 \end{Bmatrix} + \begin{bmatrix} K_{11} & K_{12} \\ \text{---} & \text{---} \\ K_{21} & K_{22} \end{bmatrix} \begin{Bmatrix} X_1 \\ \text{---} \\ X_2 \end{Bmatrix} = \begin{Bmatrix} F_1(t) \\ \text{---} \\ F_2(t) \end{Bmatrix} \quad (2)$$

Let $\{P\}$ be the $n \times 1$ vector of resultant external forces (includes applied and inertial forces). Then the relationship between resultant external forces and the displacements can be written in partitioned form as

$$\begin{Bmatrix} P_1 \\ \text{---} \\ P_2 \end{Bmatrix} = \begin{bmatrix} K_{11} & K_{12} \\ \text{---} & \text{---} \\ K_{21} & K_{22} \end{bmatrix} \begin{Bmatrix} X_1 \\ \text{---} \\ X_2 \end{Bmatrix} \quad (3)$$

Now let us define the $\{X_2\}$ displacements to be a superposition of two parts

$$\{X_2\} = \{X_2^U\} + \{X_2^C\} \quad (4)$$

where:

$\{X_2^U\}$ = displacements that occur at the $\{X_2\}$ coordinates due to $\{X_1\}$ displacements, considering the $\{X_2\}$ coordinates to be unloaded; i.e., with $\{P_2\} = 0$

$\{X_2^C\}$ = displacements that occur at the $\{X_2\}$ coordinates considering the $\{X_1\}$ displacements constrained to be zero and with the $\{X_2\}$ coordinates loaded; i.e., with $\{P_2\} \neq 0$.

Now we can determine $\{X_2^U\}$ by applying equation (3) with $\{P_2\} = 0$.

Thus,

$$\begin{Bmatrix} P_1 \\ \dots \\ 0 \end{Bmatrix} = \begin{bmatrix} K_{11} & K_{12} \\ \dots & \dots \\ K_{21} & K_{22} \end{bmatrix} \begin{Bmatrix} X_1 \\ \dots \\ X_2^U \end{Bmatrix} \quad (5)$$

It follows from equation (5) that _____

$$\{X_2^U\} = [\beta] \{X_1\} \quad (6)$$

where:

$$[\beta] = - [K_{22}]^{-1} [K_{21}] \quad (7)$$

In view of equations (6) and (7), we can now write equation (4) as

$$\{X_2\} = [\beta] \{X_1\} + \{X_2^C\} \quad (8)$$

With equation (8) we can now write the transformation equation in the form

$$\begin{Bmatrix} X_1 \\ \hline X_2 \end{Bmatrix} = \begin{bmatrix} I & | & O \\ \hline \beta I & | & I \end{bmatrix} \begin{Bmatrix} X_1 \\ \hline X_2^C \end{Bmatrix} \quad (9)$$

or more simply

$$\{X\} = [\gamma] \{Y\} \quad (10)$$

where:

$$[\gamma] = \begin{bmatrix} I & | & O \\ \hline \beta I & | & I \end{bmatrix} \quad (11)$$

$$\{Y\} = \begin{Bmatrix} X_1 \\ \hline X_2^C \end{Bmatrix} \quad (12)$$

Applying the transformation (10) to the equation of motion (1), we obtain

$$[\gamma]^T [M] [\gamma] \{\ddot{Y}\} + [\gamma]^T [C] [\gamma] \{\dot{Y}\} + [\gamma]^T [K] [\gamma] \{Y\} = [\gamma]^T \{F\} \quad (13)$$

Now equation (13) can be expanded by expressing each of the matrices in their partitioned form and carrying out the multiplication of the matrix triple products. The following equation is obtained.

$$\begin{bmatrix} M_{11}^* & | & M_{12}^* \\ \hline M_{21}^* & | & M_{22}^* \end{bmatrix} \begin{Bmatrix} \ddot{X}_1 \\ \hline \ddot{X}_2^C \end{Bmatrix} + \begin{bmatrix} C_{11}^* & | & C_{12}^* \\ \hline C_{21}^* & | & C_{22}^* \end{bmatrix} \begin{Bmatrix} \dot{X}_1 \\ \hline \dot{X}_2^C \end{Bmatrix} + \begin{bmatrix} K_{11}^* & | & K_{12}^* \\ \hline K_{21}^* & | & K_{22}^* \end{bmatrix} \begin{Bmatrix} X_1 \\ \hline X_2^C \end{Bmatrix} = \begin{Bmatrix} F_1 + \beta^T F_2 \\ \hline F_2 \end{Bmatrix} \quad (14)$$

where:

$$[M_{11}^*] = [M_{11}] + [\beta]^T [M_{21}] + [M_{12}] [\beta] + [\beta]^T [M_{22}] [\beta] \quad (15)$$

$$[M_{12}^*] = [M_{12}] + [\beta]^T [M_{22}] \quad (16)$$

$$[M_{21}^*] = [M_{21}] + [M_{22}] [\beta] \quad (17)$$

$$[M_{22}^*] = [M_{22}] \quad (18)$$

The partitions $[C_{ij}^*]$ and $[K_{ij}^*]$ have the same form as equations (15) through (18). That is

$$[C_{11}^*] = [C_{11}] + [\beta]^T [C_{21}] + [C_{12}] [\beta] + [\beta]^T [C_{22}] [\beta]$$

$$[K_{11}^*] = [K_{11}] + [\beta]^T [K_{21}] + [K_{12}] [\beta] + [\beta]^T [K_{22}] [\beta]$$

etc.

Since the $\{X_1\}$ displacements are known or prescribed, we need consider only the matrix equation from (14) describing the $\{X_2^C\}$ variable, that is

$$[M_{22}^*] \{\ddot{X}_2^C\} + [C_{22}^*] \{\dot{X}_2^C\} + [K_{22}^*] \{X_2^C\} = \{F_2\} - [M_{21}^*] \{\ddot{X}_1\} - [C_{21}^*] \{\dot{X}_1\} - [K_{21}^*] \{X_1\} \quad (19)$$

We can expand equation (19), replacing the coefficient matrices by the relationships as described in equations (15) through (18). Thus, equation (19) becomes

$$\begin{aligned} [M_{22}] \{\ddot{X}_2^C\} + [C_{22}] \{\dot{X}_2^C\} + [K_{22}] \{X_2^C\} &= \{F_2\} - [M_{21}] \{\ddot{X}_1\} - [M_{22}] [\beta] \{\ddot{X}_1\} \\ &- [C_{21}] \{\dot{X}_1\} - [C_{22}] [\beta] \{\dot{X}_1\} - [K_{21}] \{X_1\} - [K_{22}] [\beta] \{X_1\} \end{aligned} \quad (20)$$

In view of equation (7) the term $[K_{22}] [\beta] \{X_1\}$ appearing in equation (20) can be simplified as

$$[K_{22}] [\beta] \{X_1\} = - [K_{21}] \{X_1\} \quad (21)$$

Now let us assume (for convenience sake) that the damping matrix, $[C]$, is proportional to the stiffness matrix, i.e.,

$$[C] = \alpha [K] \quad (22)$$

Substituting equations (21) and (22) into equation (20) yields

$$[M_{22}] \{\ddot{X}_2^C\} + [C_{22}] \{\dot{X}_2^C\} + [K_{22}] \{X_2^C\} = \{F_2(t)\} - [M_{21}] \{\ddot{X}_1\} - [M_{22}] [\beta] \{\ddot{X}_1\} \quad (23)$$

The response of the discretely modeled structure subject to base motion excitation, $\{\ddot{X}_1\}$, and applied forcing function, $\{F_2(t)\}$, can be described by solution of equation (23) and its auxiliary equation (8). It is interesting to note that the left side of equation (23) represents the structure with the base motion coordinates $\{X_1\}$ constrained to zero. The base motion excitation $\{\ddot{X}_1\}$, appears in the forcing function terms on the right side of equation (23).

Usually it is more convenient to solve the equations of motion in terms of modal or normal coordinates rather than the discrete coordinates of equation (23). The transformation relating the discrete coordinates and the normal coordinates is

$$\{X_2^C\} = [\phi] \{q\} \quad (24)$$

where

$\{q\}$ = vector of normal coordinates

$[\phi]$ = transformation matrix

We choose $[\phi]$ to be the modal matrix obtained from the eigenvalue analysis of

$$[M_{22}] \{\ddot{X}_2^C\} + [K_{22}] \{X_2^C\} = \{0\} \quad (25)$$

That is, each column of $[\phi]$ is an eigenvector (mode shape) of equation (25).

Substituting equation (24) into equation (23) and premultiplying the resulting equation by $[\phi]^T$ yields

$$[M_{eq}] \{\ddot{q}\} + [2\zeta\omega] [M_{eq}] \{\dot{q}\} + [\omega^2] [M_{eq}] \{q\} = [\phi]^T (\{F_2\} - [M_{21}] \{\ddot{X}_1\} - [M_{22}] [\beta] \{\ddot{X}_1\}) \quad (26)$$

where $[M_{eq}]$, $[2\zeta\omega]$, and $[\omega^2]$ are diagonal matrices given as (Ref. Hurty & Rubenstein)

$$[M_{eq}] = [\phi]^T [M_{22}] [\phi]$$

$$[2\zeta\omega] [M_{eq}] = [\phi]^T [C_{22}] [\phi]$$

$$[\omega^2] [M_{eq}] = [\phi]^T [K_{22}] [\phi]$$

Now equation (26) is a very convenient form for numerical solution. In view of equations (8) and (24), the displacements $\{X_2\}$ can be determined as

$$\{X_2\} = [\beta] \{X_1\} + [\phi] \{q\} \quad (27)$$

Thus, the response of the discretely modeled structure subject to base motion excitation can also be determined by evaluating equations (26) and (27).

REFERENCES

1. Morton Thiokol Drawing No. IU50129, "Case Segment, AFT," dated January 23, 1977.
2. Morton Thiokol Drawing No. IU50088, "Housing, Nozzle-Fixed," dated July 3, 1974.
3. Morton Thiokol Drawing No. IU50145, "Segment, Rocket Motor-AFT," dated July 8, 1979.
4. Morton Thiokol Drawing No. IU52945, "Housing Nozzle-Fixed," dated October 2, 1986.
5. Morton Thiokol Document No. TWR-13088, "Natural Frequency of the Space Shuttle SRM High Performance Motor Nozzle," dated July 9, 1981.
6. Morton Thiokol Document No. TWR-13605, "Space Shuttle SRM Nozzle Structural Dynamic Characteristics," dated December 1, 1982.
7. Morton Thiokol Memorandum EL60/CAS-FY88-448, "SRB Nozzle Redesign Loads," dated May 13, 1988.
8. NASA Report No. SE019-0572H, "SRB Design Loads Data Book," Latest Copy Book 1.
9. Morton Thiokol Memorandum EL60/CAS-FY87-43, "SRM Chamber Pressure Drop Data," dated October 15, 1986.
10. Morton Thiokol Document No. TWR-300107, "Calculated Axial Pressure Distributions During the Ignition Transient," dated March 19, 1986.
11. Morton Thiokol Report No. CTP-0006, "Transient Pressure Test Article (TPTA) 1.1 Test Plan," dated November 2, 1987.
12. Morton Thiokol Drawing No. 7075234, "Instrumentation Installation Kit, TPTA," dated September 15, 1987.
13. Rockwell Report No. IL280-201-87-040, "Liftoff Loads for Design Certification Review," dated June 2, 1987.

APPROVAL

**STATIC AND DYNAMIC DEFLECTION STUDIES OF THE
SRM AFT CASE/NOZZLE JOINT**

By D.C. Christian, L.D. Kos, and I. Torres

The information in this report has been reviewed for technical content. Review of any information concerning Department of Defense or nuclear energy activities or programs has been made by the MSFC Security Classification Officer. This report, in its entirety, has been determined to be unclassified.



JAMES C. BLAIR
Director, Structures and Dynamics Laboratory